

Tuning the properties of pineapple peel cellulose nanofibrils by TEMPO-mediated oxidation and ball milling

Tianyi Lv

Southwest University

Yuan Chen

Southwest University

Yuyuan Luo

Southwest University

Difei Dai

Southwest University

Xin Feng

Southwest University

Hai Chen

Southwest University

Yong Yu

Southwest University

Liang Ma

Southwest University

Yuhao Zhang

Southwest University

Hongjie Dai (✉ daihjdemo@163.com)

Southwest University <https://orcid.org/0000-0002-5541-0301>

Research Article

Keywords: Pineapple peel, Cellulose nanofibrils, TEMPO oxidation, Ball milling, Aerogel

Posted Date: May 11th, 2022

DOI: <https://doi.org/10.21203/rs.3.rs-1530006/v1>

License:   This work is licensed under a Creative Commons Attribution 4.0 International License.

[Read Full License](#)

Abstract

In this study, the oxidized cellulose nanofibrils from pineapple peel (PP-TOCNF) were prepared by TEMPO-mediated oxidation followed by ball milling. The influence of oxidation degree on the structure and properties of PP-TOCNF were investigated, including Fourier transform infrared spectroscopy (FTIR), X-ray diffraction (XRD), atomic force microscope (AFM), X-ray photoelectron spectroscopy (XPS) and thermogravimetry (TG), as well as the potential application in aerogels. The results suggested that TEMPO oxidation facilitated the dispersion of PP-TOCNF due to the strong electrostatic repulsion between $-COO^-$ groups. Regulating oxidation degree by varying NaClO concentration could effectively adjust the $-COO^-$ content (0.167 ~ 0.550 mmol/g), zeta potential (-18 ~ -34 mV) and rheological properties. The obtained PP-TOCNF showed a long fibrillar structure, whose average diameter and CrI values gradually decreased with the increase of oxidation degree. The PP-TOCNF-based aerogels exhibited a light weight, good porosity, water absorption, and mechanical properties, which also can be easily adjusted by oxidation degree of PP-TOCNF. Furthermore, TEMPO oxidation improved the stability and shape recovery ability of aerogels in water.

Introduction

Tremendous energy consumption has been considered as one of the most serious social problems, which is an urgent need and demand for developing more energy efficient, more affordable and more sustainable resources. Cellulose, as the most abundant renewable biopolymer on Earth, is mainly derived from agricultural and forest residues and considered to be a promising candidate (Dai et al. 2020), due to its superior characteristics of wide source, low-cost and environmental friendliness (Dilamian et al. 2021). Considering the insolubility of natural cellulose, the effective utilization of cellulose is mainly through chemical modification to form cellulose derivatives (Mettu et al. 2021) (e.g., carboxymethyl cellulose (CMC), methylcellulose (MC), hydroxypropyl methylcellulose (HPMC), cellulose acetate (CA), and hydroxyethyl cellulose (HEC) (Cho et al. 2021)), or through micro/nano processing to form microcrystalline cellulose (MCC) or nanocellulose (Dai et al. 2021). Among these, nanocellulose is gaining tremendous research attention due to its superior properties such as renewability, biodegradability, biocompatibility, high aspect ratio, high specific surface area, easy availability, high mechanical strength, and good modifiability (Sun et al. 2021).

Generally, nanocellulose can be divided into three main types, namely cellulose nanocrystals (CNCs), cellulose nanofibrils (CNFs) and bacterial cellulose (BC) depending on their sizes, resources and preparation techniques (Dai et al. 2020). Among these, CNFs as longer semi-flexible fibrils have been gaining considerable attention for their attractive features, such as low cost, gentle extraction method, high aspect ratio, gel-like behavior, and industrialized production potential (Perumal et al. 2022). Recently, CNFs have been regarded as a promising material for applications in stabilizer, food packing, papermaking and nanocomposites (Poyraz et al. 2018; Yang et al. 2020).

The application of CNFs mainly depends on its preparation method, which influences its properties such as morphology, crystallinity and surface properties. At present, the common methods for CNF isolation include high pressure homogenization, microfluidization, sonication and mechanical grinding (Chen et al. 2021). However, due to the strong inter- and intramolecular hydrogen bonds among cellulose chains, the enormous energy and time consumption during mechanical disintegration process are always a challenge in CNF isolation. Recently, some studies have found that effective pretreatments can reduce energy consumption to facilitate the disintegration and nanofibrillation of cellulose, such as chemical modification, enzymatic pretreatments (Perzon et al. 2020), and alkali treatment (Miao et al. 2016). For CNF production, the TEMPO (2,2,6,6-tetramethylpiperidine-1-oxyl)-mediated oxidation of native cellulose stands out amongst the most used chemical methods, showing advantages in terms of individual fibers, uniform size, long length and flexible (Van Hai et al. 2018). Furthermore, the TEMPO-mediated oxidation can result in the regioselective conversion of the hydroxyl groups at the C6 positions of cellulose molecules into carboxylic groups, thus endowing CNFs with improved dispersibility in water (Qu et al. 2021).

Aerogel is a highly porous nanostructured material with characteristics of high porosity, high surface area and low density (Wan et al. 2019), which has been regarded as a promising material for a variety of applications such as biomedical scaffolds, separation and adsorption, among others (Liu et al. 2021). Cellulose aerogel is known as a new generation of aerogel material following inorganic aerogel and organic polymer aerogel, and it combines the traditional properties of aerogels with the advantages of cellulose and belongs a promising material for making aerogel with flexibility and pressure resistance. The carboxyl groups of CNFs induced by TEMPO-mediated oxidation can improve the properties of CNF aerogel due to the electrostatic repulsion between cellulose fibers, thus preventing the pores from collapsing (Gong et al. 2021). The oxidation degree can effectively dominate the properties of CNFs, which is of great significance for the application of CNF aerogel. However, there is still a lack of information available on the effect of degree of oxidation.

Pineapple is the third most important tropical fruit in the world with an annual output of 28 million tons, whose consumption produces a lot of wastes (e.g., leaf, stem and peel) accounting for 50% (w/w) of total fruit mass (Shivamathi et al. 2022). Recently, our research team has confirmed the feasibility of pineapple peel as a raw material for cellulose and nanocellulose extraction (Dai et al. 2018), whose potential applications involve the fields of hydrogels (Dai et al. 2017), emulsion stabilizer (Dai et al. 2021), adsorbents (Dai et al. 2019), controlled drug release (Dai et al. 2019), etc. However, the isolation of CNFs from pineapple peel and its TEMPO oxidation have not been reported yet to the best of our knowledge. In this study, the pineapple peel, as raw material was used to prepare CNFs by TEMPO-mediated oxidation followed by ball milling. The influence oxidation degree on the physical and chemical properties of CNFs and its application in aerogels were investigated systemically.

Materials And Methods

Materials and reagents

Pineapple peel was freely provided by a pineapple processing factory in Zhanjiang (Guangdong Province, China), and then used to isolate from cellulose (PPC) according to our previous study (Dai et al. 2019). Sodium hydroxide (NaOH), sodium bromide (NaBr), Hydrochloric acid (HCl) and ethanol were purchased from Kelong Reagent Co., Ltd. (Chengdu, China). Sodium chlorite (NaClO₂) and TEMPO were provided by Yuexiang Chemical Co., Ltd. (Chongqing, China). Sodium hypochlorite (NaClO) solution with the available chlorine of 10 ~ 15% was purchased from Jiuding Chemical Technology Co., Ltd. (Chongqing, China). All other chemical reagents were of analytical grade without further purification.

Preparation of TEMPO-oxidized pineapple peel CNFs (PP-TOCNF)

PP-TOCNF was obtained according to TEMPO-mediated oxidation followed by mechanical ball milling (Huang et al. 2020). Briefly, 1 g of PPC was suspended in 100 mL of distilled water containing TEMPO (0.0125 g) and NaBr (0.125 g). Then, the TEMPO-mediated oxidation of the PPC slurry was initiated after adding various amounts of NaClO (2.5, 5 and 10 mmol) at 25°C and pH 10 during 1.5 h reaction at room temperature. Lastly, the resulting slurry was collected and dialyzed at 4°C for 3 d to gain the oxidized PPC (TOPPC). Afterwards, the obtained TOPPC was further ball milled using a vertical planetary ball mill (XQM-0.4A, Tencan powder, China). Briefly, the TOPPC (1.0%, 20 mL) and zirconia balls (90 g) with different diameters (15, 12, 10, 8 and 5 mm) in the zirconia ball mill jar. The ball milling was processed at a speed of 400 rpm for 3 h at room temperature and performed in cycles of 20 min/milling per 10 min/rest. Then, the resulting slurry was collected and washed by three repeated centrifugation (5000 r/min, 10 min) and dispersed by ultrasonic treatment (300 W, 30 min). The obtained suspension was stored at 4°C for further use or freeze-dried for characterization. According to the addition of NaClO, the obtained PP-TOCNF samples were coded as PP-TOCNF-2.5, PP-TOCNF-5, and PP-TOCNF-10, respectively. As a control, the pineapple peel CNFs (PP-CNF) were also prepared by directly ball milling method without TEMPO-mediated oxidation. The carboxylate content of PP-TOCNF was determined by a conductometric titration procedure using a conductivity meter (FE38, Mettler Toledo, Switzerland).

Zeta potential measurement

Zeta potentials of PP-CNF and PP-TOCNF suspensions (0.05%, w/w) were measured by a Zetasizer Nano ZS particle analyzer (Malvern Instrument, UK) at 25°C. Before analysis, the suspensions were ultrasonically treated for 10 min.

UV/visible (UV-Vis) light transmittances

The UV-Vis light transmittances of PP-CNF and PP-TOCNF suspensions (0.02%, w/w) were recorded by a UV-Vis spectrophotometer (UV 6100, Metash, China) in the wavelength range 200 ~ 900 nm. The transmittance spectra were attained by means of cuvette as background.

Fourier transform infrared spectroscopy (FTIR)

FTIR spectra of samples were recorded using a Fourier transform infrared spectrometer (Thermo Nicolet iS10, Thermo Fisher Scientific, USA) in the range of 4000 ~ 600 cm^{-1} with a resolution of 4 cm^{-1} and 32 scans.

Atomic force microscopy (AFM)

Topographical characterization of PP-CNF and PP-TOCNF was obtained using an atomic force microscope (Cypher ES, Oxford Instruments, USA). Before observation, the diluted suspension (0.01%) was dropped on the mica substrate and air-dried at room temperature. The average value and distribution of diameter were analyzed by the Nano Measurer 1.2 software.

X-ray diffraction (XRD)

The crystalline structure of samples was analyzed by an X-ray diffractometer (X'Pert3 Powder, Malvern Panalytical, Netherlands), with a Ni-filtered Cu-K α radiation ($\lambda = 0.15444 \text{ nm}$) operating at an anode voltage of 40 kV and a current of 40 mA. The XRD data were collected in the 2θ range from 10° to 40° with a scan rate of $4^\circ/\text{min}$. The crystallinity index (CrI) was calculated by the Segal's method (Segal et al. 1959):

$$CrI(\%) = \frac{I_{200} - I_{am}}{I_{200}} \times 100$$

1

where I_{200} is the maximum intensity of the (200 plane) diffraction peak, and I_{am} is the minimum diffraction intensity for amorphous region between planar reflections (200) and (110).

X-ray photoelectron spectroscopy (XPS)

XPS spectra of PP-CNF and PP-TOCNF were recorded using an XPS spectrometer (Scientific K-Alpha, Thermo, USA) using an Al K α X-ray irradiation ($h\nu = 1486.6 \text{ eV}$). Low-resolution survey spectra were recorded in 1 eV steps and pass energy of 100 eV. The high-resolution of the C 1s spectra (278 ~ 294 eV) and the O 1s spectra (525 ~ 545 eV) were recorded in a step size of 0.05 eV and a pass energy of 50 eV (Payormhorm et al. 2020).

Thermal stability analysis

The thermal stability of samples was analyzed by a thermogravimetric analyzer (TGA550, TA Instruments, USA) with temperature range from 30 to 600°C at a constant heating rate of $10^\circ\text{C}/\text{min}$ under a nitrogen flow of 50 mL/min.

Rheological behavior of PP-CNF and PP-TOCNF suspensions

The rheological properties of PP-CNF and PP-TOCNF suspensions (1.0%, w/v) were measured using a rotational rheometer (MCR 302, Anton Paar Physica, Austria) equipped with a parallel-plate fixture (25 mm diameter). The linear viscoelastic region of samples was measured with a strain sweep (γ) of 0.01 ~ 100% in an oscillatory mode, and the viscosity and the dynamic frequency sweep of samples were performed at an increasing shear rate from 0.1 to 100 s^{-1} . All measurements were performed at a gap of 1.0 mm within the linear viscoelastic region at a reference temperature of 25°C.

Application in aerogel

Preparation of aerogel

The aerogels were simply prepared by a direct freeze-drying method (Manzocco et al. 2022). Briefly, the PP-CNF, PP-TOCNF-2.5, PP-TOCNF-5 and PP-TOCNF-10 suspensions (1.0%, w/w) were respectively poured into a cylindrical mold and pre-frozen by an ultra-low temperature refrigerator (-80°C, 24 h). Afterwards, the samples were lyophilized at -50°C in a freeze-drier (Heraeus Multifuge XWR, Thermo Fisher, USA) for 48 h to obtain aerogels. Correspondingly, the obtained aerogels were named as PP-CNF-AG, PP-TOCNF-2.5-AG, PP-TOCNF-5-AG, and PP-TOCNF-10-AG, respectively.

Density and porosity measurements

The density of the obtained aerogels can be calculated by the following equation:

$$\rho = \frac{M}{V}$$

2

where ρ (g/cm^3) is the density of aerogels, M (g) and V (mL) are the weight and geometric volume of aerogels, respectively.

The porosity of the obtained aerogels was determined by a liquid displacement method (Lin et al. 2012). In brief, the obtained aerogels were immersed in absolute ethanol at room temperature for 30 min to ensure complete infiltration. After gently taking out and wiping off the surface ethanol, the samples were weighed immediately. The porosity of the aerogels can be calculated by the following equation:

$$\text{Porosity}(\%) = \frac{V_p}{V_a} \times 100 = \frac{M_e - M_0}{\rho_e V_a} \times 100$$

3

where V_p (mL) and V_a (mL) are the pore volume and geometric volume of aerogels, respectively; M_e is the weight of aerogel filled with absolute ethanol, M_0 is the dry weight of aerogel, and ρ_e is the density of ethanol (0.789 g/cm^3).

Water absorption measurement

The water absorption of aerogels was measured by a gravimetric method (Metu et al. 2021). Briefly, the freeze-dried aerogel was soaked in distilled water at room temperature and taken out until the adsorption

equilibrium was achieved. After removing the surface water using a filter paper, the samples were weighed immediately. The water absorption capacity (WA) of aerogels was calculated using the following equation:

$$WA(g/g) = \frac{M_w - M_d}{M_d}$$

4

where M_w (g) is the weight of the aerogel after water adsorption, and M_d (g) is the initial weight of the dried aerogel.

Scanning electron microscopy (SEM)

The morphologies of the aerogels were observed by a scanning electron microscope (Phenom pro, Phenom-World BV, Netherlands) at an operating voltage of 10 kV. Before observation, the samples were sputter-coated with a gold-palladium.

Mechanical property analyses

The mechanical performance of the aerogels was determined by an electronic universal testing machine (E44.104, MTS, USA) equipped with a 1 KN standard load cell. The compression strain was set to 86% on the cylindrical aerogel samples with a crosshead speed of 15 mm/min.

Statistical analysis

All measurements were repeated at least 3 times. The obtained data were partially presented as mean values \pm standard deviation (SD).

Results And Discussion

Carboxylate content and yield

The carboxylate content and yield of PP-CNF and PP-TOCNF are summarized in Table 1. After TEMPO-mediated oxidation, the carboxylate content of PP-TOCNF-2.5, PP-TOCNF-5 and PP-TOCNF-10 was 0.218 ± 0.011 , 0.331 ± 0.041 and 0.550 ± 0.041 mmol/g, respectively, showing an increased oxidation degree with the increase of NaClO concentration. Accordingly, the carboxylate content of PP-TOCNF can be effectively adjusted by controlling oxidation parameters (e.g., NaClO concentration). The yield of PP-CNF, PP-TOCNF-2.5, PP-TOCNF-5 and PP-TOCNF-10 was $73.10 \pm 3.11\%$, $68.28 \pm 1.59\%$, $74.50 \pm 2.12\%$, and $75.25 \pm 0.28\%$, respectively. Compared with PP-CNF directly isolated by ball milling, the yield of PP-TOCNF firstly decreased (PP-TOCNF-2.5) and then slightly increased (PP-TOCNF-5 and PP-TOCNF-10) with the increase of oxidation degree. This trend could be caused by a combination of the increases of cellulose degradation and defibrillation degree during TEMPO-mediated oxidation and balling process (Huang et al. 2020). Under the oxidation conditions, the cellulose can be oxidized and depolymerized into water soluble derived compounds (Isogai et al. 2018). The decrease of yield at low oxidation degree is probably due to the fact that the increased defibrillation degree cannot offset the increase of amorphous region

hydrolysis of cellulose, while higher oxidation degree leads to an easier defibrillation by ball milling, thus resulting in an increase of yield (Liu et al. 2018).

Table 1
Carboxylate content and yield of PP-CNF and PP-TOCNF

Samples	n_{COOH} (mmol/g)	Yield/%
PP-CNF	/	73.70 ± 3.11^a
PP-TOCNF-2.5	0.218 ± 0.011^c	68.25 ± 1.59^b
PP-TOCNF-5	0.331 ± 0.041^b	74.50 ± 2.12^a
PP-TOCNF-10	0.550 ± 0.031^a	75.25 ± 0.18^a

Zeta potential analysis and visual appearance

The zeta potential value and visual appearance of PP-CNF and PP-TOCNF suspensions are shown in **Fig. 1a** and **b**. As shown in **Fig. 1a**, the zeta potential value of PP-CNF, PP-TOCNF-2.5, PP-TOCNF-5 and PP-TOCNF-10 was -18.13 ± 1.01 , -24.20 ± 1.65 , -26.67 ± 0.50 , and -33.90 ± 1.71 mV, respectively corresponding to the change of carboxylate content (**Table 1**). The increase of oxidation degree resulted in the increase of carboxylate content, thus endowing PP-TOCNF with better colloidal stability due to stronger electrostatic interaction between carboxyl groups (Yang et al. 2019). As shown in **Fig. 1b**, after standing for 1 d at room temperature, all samples showed a delamination at a low concentration (0.1%), implying a poor colloidal stability. However, with the increase of solid concentration (0.5% and 1%), the colloidal stability was visibly enhanced due to the increase of electrostatic repulsion and solution viscosity (Li et al. 2015). Notably, all the PP-TOCNF samples showed a better colloidal stability than that of PP-CNF, mainly attributing to the enhanced electrostatic repulsion.

FTIR analysis

FTIR spectra of PPC, PP-CNF, and PP-TOCNF are shown in **Fig. 1c**. All samples displayed the characteristic peaks of cellulose I structure at 3300, 2929, 1620, 1425, 1370, 1050 and 896 cm^{-1} , indicating the chemical structure of cellulose can be maintained after TEMPO oxidation and ball milling process. The peak at around 3300 cm^{-1} reflected the intramolecular -OH bond stretching vibration. The narrow peak at 2929 cm^{-1} belonged to the C-H stretching vibration, and the peaks at 1425 and 1050 cm^{-1} represented the stretching vibration of C-O-C (Zhao et al. 2017). The peaks around 1370 and 896 cm^{-1} were attributed to the stretching vibrations of the β -glycosidic bond between the glucose units of the cellulose molecule (Hassan et al. 2021). Compared with PPC, PP-CNF directly obtained by ball milling showed a higher intensity at 896 cm^{-1} , corresponding to a higher level of glycosidic linkages between

glucose units in cellulose (Sofla et al. 2016). After TEMPO-mediated oxidation, the obtained PP-TOCNF showed an increased peak intensity around 1620 cm^{-1} that belongs to the stretching vibration of C=O (Lyu et al. 2021), implying the increase of oxidation degree, which is consistent with the results of carboxylate content (**Table 1**).

UV-Vis light transmittances analysis

The light transmittances of PP-CNF and PP-TOCNF suspensions are shown in Fig. 1d. As can be clearly observed from this figure, all PP-TOCNF samples showed a better light transmittance than that of PP-CNF. The increase in light transmittance was positively correlated with the increase in the oxidation degree of PP-TOCNF, showing the highest light transmittance in PP-TOCNF-10. The higher carboxyl groups on the surface of PP-TOCNF can increase the electrostatic repulsion between nanofibrils, thus improving the dispersion properties of suspensions and the light transmittance (Besbes et al. 2011). In addition, the transmittance of the suspension is also closely related to the particle size of the substance (Levanič et al. 2020), which implied the decrease of particle size of PP-TOCNF with increasing oxidation degree, which can be confirmed by the following result of AFM (Fig. 2).

Morphological analysis

The AFM images and diameter distributions of PP-CNF, PP-TOCNF-2.5, PP-TOCNF-5, and PP-TOCNF-10 are depicted in Fig. 2. All samples showed a long fibrillar structure in their AFM images, belonging to typical morphological structure of CNFs. After ball milling, the PPC can be separated into individual nanofibril to generate PP-CNF, showing an average diameter of 42.31 nm. Notably, after TEMPO oxidation followed by ball milling, the average diameter of the obtained PP-TOCNF gradually decreased with the increase of oxidation degree, showing an average value of 32.36 nm for PP-TOCNF-2.5, 18.68 nm for PP-TOCNF-5, and 17.00 nm for PP-TOCNF-10, respectively. The surface carboxyl groups of PP-TOCNF could reduce the adhesion by forming strong electrostatic repulsion among nanofibrils (Lai et al. 2014). And it is related to the increase of zeta potential, which can enhance the electrostatic repulsion between nanofibrils to promote the nanofibril disaggregation (Huang et al. 2019).

XRD analysis

XRD patterns of PPC, PP-CNF, and PP-TOCNF samples are displayed in Fig. 3a, and their corresponding Crl values are shown in Fig. 3b. All samples showed some similar diffraction peaks at 2θ of around 16.0° , 22.8° and 34.5° , respectively corresponding to (110), (200) and (004) of the cellulose I β crystal structure (Mhd Haniffa et al. 2017), indicating the crystal structure of PP-CNF and PP-TOCNF can be maintained after TEMPO oxidation and ball milling. Compared with the Crl value of PPC (32.52%), the Crl value of PP-CNF was significantly reduced (21.58%), which could be attribute to the disruption of crystalline order of CNFs by the ball-milling-imposed mechanical stress (Khan et al. 2015). The Crl value of PP-TOCNF-2.5, PP-TOCNF-5 and PP-TOCNF-10 was 24.16%, 30.03% and 34.56%, respectively. The Crl value of PP-TOCNF increased with the degree of oxidation increase, attributing to the destruction of amorphous region during TEMPO oxidation process (Tang et al. 2017). In addition, the TEMPO-mediated oxidation can make the

structure of PPC loose, thereby resulting in an easier removal of the amorphous region during the ball milling (Qu et al. 2021).

XPS analysis

The surface elemental composition of PPC, PP-CNF, and PP-TOCNF can be reflected by XPS, and the results are shown in Fig. 3c-i. As shown in Fig. 3c, the XPS survey spectra exhibited two main peaks, respectively at 532 eV for O 1s and 286 eV for C 1s. Compared with the O/C ratio of PPC (0.396), the O/C ratio of PP-CNF (0.522) was significantly increased, attributing to the exposure of more hydroxyl groups during ball milling. After TEMPO oxidation followed by ball milling, the O/C ratio of PP-TOCNF-2.5, PP-TOCNF-5 and PP-TOCNF-10 was 0.580, 0.597, and 0.604, respectively, showing a further increase of O/C ratio with the increase of oxidation degree, which can be attributed to the formation of carboxyl groups in PP-TOCNF. Notably, there was no significant difference in O/C values among PP-TOCNF samples. The oxidation occurred at the surface of cellulose at low NaClO concentration (2.5 mmol), and gradually further occurred at both on the surface and greater depth area of cellulose with higher NaClO concentration, but it cannot be revealed by surface elemental analysis (Lai et al. 2013). As shown in Fig. 3d-h, the C 1s survey spectra of all samples showed three peaks at 284.50, 286.10 and 287.40 eV, respectively belonging to C-C/C-H, C-O and O-C-O/C = O groups (Fei et al. 2020). Compared with the peak area of C-O for PPC (34.50%), PP-CNF increased to 43.87%, attributing to more exposure of hydroxyl groups during the defibrillation process by ball milling. The peak area of C-O and O-C-O/C = O for PP-CNF and PP-TOCNF remained almost unchanged. This trend might be due to the combination effects of TEMPO-mediated oxidation and ball milling. As the amount of C-O can be increased during ball milling and the amount of C = O also can be increased by TEMPO oxidation, the relative percentages of these two functional groups will affect each other and influence these peaks. The O 1s survey spectra of all samples is shown in Fig. 3i. The peak at 533 eV for PPC and PP-CNF belonged to the O-C groups, and the peak around 532.5 eV for PP-TOCNFs was attributed to the O = C groups, also confirming the introduction of carboxyl groups (Barazzouk et al. 2011).

Thermal stability analysis

The thermal stability of PPC, PP-CNF, and PP-TOCNF samples was analyzed by the thermogravimetric analysis (TGA) and the derivative thermogravimetric analysis (DTG), and the results are shown in Fig. 4a-b. The first peak below 100°C was due to the weight loss of residual moisture in samples (Dai et al. 2018). PPC and PP-CNF respectively started to decompose at 222.79 and 206.64°C (T_{onset}), and reached the maximum degradation rate at 326.91 and 322.13°C (T_{max}). Compared with PPC, the lower degradation temperature of PP-CNF could be attributed to its more available surface area for chemical reaction and lower CrI value (Sofla et al. 2016). PP-TOCNF also showed a decreased trend in T_{onset} and T_{max} , showing 202.91 and 305.07°C for PP-TOCNF-2.5, 183.64 and 299.78°C for PP-TOCNF-5 and 175.68 and 290.54°C for PP-TOCNF-10, respectively. This trend is due to the existence of carboxyl groups in PP-TOCNF (Masruchin et al. 2018). As for PP-TOCNF samples, the thermal degradation involves several chemical reaction, including dehydration, hydrolysis, depolymerization, decarboxylation and

transglycosylation reaction (Gómez et al. 2016). At the second stage, PP-TOCNF showed two thermal decomposition steps. The first degradation peak at 200 ~ 250°C was ascribed to the decarboxylation of the carboxyl groups, and the second degradation peak that occurred at 250 ~ 300°C was due to the thermal decomposition of PP-TOCNF (Kim et al. 2021).

Rheological analysis

Figure 5a shows the curves for elastic modulus (G') and the loss modulus (G'') versus the imposed shear strain (γ) of PP-CNF and PP-TOCNF suspensions (1.0%, w/v). The strain sweep test was used to confirm the linear viscoelastic region of samples. As can be seen from this figure, the G' and G'' values of all samples were stable at $\gamma = 0.1\%$, so it was selected in the subsequent test. The shear rate-viscosity and frequency-modulus curves of PP-CNF, PP-TOCNF-2.5, PP-TOCNF-5 and PP-TOCNF-10 are displayed in Fig. 5b. It can be seen that in the shear rate range of 0.1–100%, as the shear rate gradually increased, the viscosity of suspensions gradually decreased, showing a typical shear thinning behavior as a non-Newtonian fluid. The three-dimensional network structure of the entangled or aggregated CNFs can be destroyed during the shearing process, thus reducing the fluid resistance and its apparent viscosity (Malkin 2013). And it can be obviously observed that the viscosity of PP-TOCNF increased with the increase of oxidation degree, attributing to the viscosity mainly depends on the carboxyl content and morphology (Wei et al. 2017).

The G' and G'' of PP-CNF and PP-TOCNF suspensions as a function of angular frequency ($\omega = 0.1 \sim 100$ rad/s) are shown in Fig. 5c. The values of G' and G'' increased with the increase of frequency. At low frequency (0.1 ~ 10 rad/s), the G' values of all samples were higher than G'' values, showing a gel network structure formation in the suspensions. At high frequency (10 ~ 100 rad/s), the G' values of PP-TOCNF were still higher than their G'' values, but the PP-CNF sample occurred a cross-over point, displaying a quasi-liquid behavior at high frequency. In general, it is a sign of gelation that existing a cross-over point where $G' = G''$ (Ding et al. 2018). Therefore, PP-CNF and PP-TOCNF can form the elastic 3D network and have the potential of gelation. As depicted in Fig. 5d, the PP-CNF sample exhibited a stronger liquidity, but the liquidity of PP-TOCNF decreased with the increase of oxidation degree, showing an obvious gelation behavior (especially in PP-TOCNF-10).

Application in aerogel

Density, porosity and water absorption of aerogel

The density, porosity and water absorption (WA) values for PP-CNF-AG and PP-TOCNF-AG are summarized in Table 2. Compared with the density of PP-CNF-AG (0.0156 g/cm³), the density of PP-TOCNF-AG samples showed a decreased trend (0.0097 ~ 0.0136 g/cm³). It can be observed that the density of aerogel firstly decreased and then increased with the increase of oxidation degree, attributing to the electrostatic interaction between the nanocellulose filaments in the suspension. The increase in the density of PP-TOCNF-10-AG might be due to the high carboxyl content that formed a dense structure

(Gong et al. 2021). Compared with the porosity of PP-CNF-AG (75.30%), the porosity of PP-TOCNF-AG samples increased visibly (79.76% ~ 86.97%) and reached a stable value for PP-TOCNF-5-AG and PP-TOCNF-10-AG. The water absorption values of PP-CNF-AG, PP-TOCNF-2.5-AG, PP-TOCNF-5-AG and PP-TOCNF-10-AG aerogel were 38.18, 46.37, 70.71 and 56.28 g/g, respectively, showing an inverse relationship with aerogel densities, which was also reported in other study (Zhang et al. 2016).

Table 2
Density, porosity and water absorption of aerogel (PP-CNF-AG, PP-TOCNF-2.5-AG, PP-TOCNF-5-AG and PP-TOCNF-10-AG)

Samples	Density (g/cm ³)	Porosity (%)	WA (g/g)
PP-CNF-AG	0.0156 ± 0.0001 ^a	75.30 ± 0.57 ^c	38.18 ± 0.23 ^d
PP-TOCNF-2.5-AG	0.0136 ± 0.0003 ^b	79.76 ± 1.10 ^b	46.37 ± 1.63 ^c
PP-TOCNF-5-AG	0.0097 ± 0.0001 ^d	86.97 ± 1.02 ^a	70.71 ± 0.76 ^a
PP-TOCNF-10-AG	0.0120 ± 0.0003 ^c	85.68 ± 0.72 ^a	56.28 ± 1.86 ^b

SEM analysis

The surface morphological structure of PP-CNF-AG, PP-TOCNF-2.5-AG, PP-TOCNF-5-AG and PP-TOCNF-10-AG are shown in Fig. 6a. As can be clearly observed from this figure, the surface morphologies of aerogels can be influenced by TEMPO oxidation with different oxidation degree. Obviously, PP-CNF-AG exhibited a randomly stacked structure of fragments, while the PP-TOCNF-AG samples showed an obvious entangled porous network structure. Notably, as the oxidation degree increased, the network structure and surface of PP-TOCNF-AG became tighter. This might be because the PP-TOCNF-AG surface contained lots of carboxyl groups, which enhanced the electrostatic interaction between the particles. As the repulsive force between particles increased, the distance between particles was eliminated thus leading to the smaller pores, and some aggregation might be occurred thus forming the lamellar structure (Sehaqui et al. 2011). However, due to the formation of lamellar structure, some properties of aerogel such as water absorption will be limited to a certain extent. Thus, the proper use of TEMPO-mediated oxidation to introduce negative charge is necessary for the further application of CNFs.

Mechanical property analyses

Figure 6b is a digital photograph of the appearance of the obtained aerogel, showing a typical light weight characteristic of aerogel that can be placed smoothly over the flower. The compression test was used to analyze the mechanical characteristics of the obtained aerogels, and the results are shown in Fig. 6c. There was no yield occurred at a strain of up to 86%, which was a typical deformation behavior of porous materials (Mirtaghavi et al. 2020). When the strain reached 86%, the compressive stress of PP-

CNF-AG was 37.67 kPa, the compression stress values of PP-TOCNF-2.5-AG, PP-TOCNF-5-AG and PP-TOCNF-10-AG were 34.16, 18.13 and 14.45 kPa, respectively. It can be demonstrated that TEMPO oxidation may regulate the mechanical characteristics of aerogel, with compressive strength decreasing and flexibility increasing as the degree of oxidation rose (Chen et al. 2019). That might be because CNFs tend to be ordered, making the aerogel structure fluffy and thereby decreasing its compression resistance. The force change process of aerogel can be divided into three parts: (a) when strain (ϵ) < 40%, it was a linear elastic zone, the compression stress (σ) remained almost unchanged, and the deformation was mainly caused by the flexibility of cellulose; (b) when 40% < ϵ < 60%, it was a plateau area, and the σ increased linearly with the increase of ϵ , suggesting that the network structure of aerogel bear a certain stress; (c) when ϵ > 60%, it was the densification stage, and the σ increased rapidly, indicating that the inter-fiber pores inside the aerogel were highly compressed and became dense, that is, plastic deformation had occurred (Li et al. 2016). As can be obviously seen in Fig. 6d, all aerogel samples maintained their initial shape after being soaked in water for 1 h. However, after prolonging to 12 h, PP-CNF-AG was dissociated while PP-TOCNF-AG still remains its initial shape, showing a better structural integrity in aqueous solutions. In addition, compared with PP-CNF-AG, the PP-TOCNF-AG samples had better rehydration performance after pressed. These results suggest TEMPO oxidation endows CNF aerogel with better structural stability and shape recovery ability, providing tuning potential for their aerogel applications.

Conclusion

CNFs were successfully defibrillated from pineapple peel using TEMPO-mediated oxidation treatment followed by ball milling. TEMPO oxidation endowed CNFs with desirable dispersion and suspension stability in water and good gel-forming ability. The results of FTIR, XPS and XRD implied that the basic chemical structure of PP-CNF can be maintained after TEMPO oxidation procedure. The obtained PP-TOCNF showed a long fibrillar structure and the average diameter gradually decreased with the increase of oxidation degree. Furthermore, controlling TEMPO oxidation degree can effectively adjust the porosity, water absorption and mechanical properties of PP-TOCNF aerogels. This work emphasized the effective approach of oxidation degree on the adjustment of the properties of CNFs.

Declarations

Author contributions Tianyi Lv: Methodology, Investigation, Visualization, Writing-Original Draft. Yuyuan Luo: Investigation, Resources. Yuan Chen: Investigation, Resources. Difei Dai: Investigation, Resources. Xin Feng: Formal analysis. Hai Chen: Visualization. YongYu: Visualization. Liang Ma: Supervision, Project administration. Yuhao Zhang: Conceptualization, Funding acquisition. Hongjie Dai: Conceptualization, Funding acquisition.

Funding This study was supported by the National Natural Science Foundation of China (No. 31901683), Natural Science Foundation of Chongqing, China (No. cstc2020jcyj-msxmX0087), National Key R&D

Program of China (No. 2021YFD2100105), and the Ecological Fishery Technological System of Chongqing Municipal Agricultural and Rural Committee under Grant.

Data availability All the data used to support the findings of this study are included within the article.

Compliance with ethical standards

Conflict of interest The authors declare that they have no conflicts of interest.

Ethical approval This study does not contain any studies with human participants or animals performed by any of the authors.

References

1. Barazzouk S, Daneault C (2011) Tryptophan-based peptides grafted onto oxidized nanocellulose. *Cellulose* 19:481–493. <https://doi.org/10.1007/s10570-011-9633-9>
2. Besbes I, Alila S, Boufi S (2011) Nanofibrillated cellulose from TEMPO-oxidized eucalyptus fibres: Effect of the carboxyl content. *Carbohydr Polym* 84:975–983. <https://doi.org/10.1016/j.carbpol.2010.12.052>
3. Chen Y, Fan D, Lyu S, Li G et al (2019) Elasticity-Enhanced and aligned structure nanocellulose foam-like aerogel assembled with cooperation of chemical art and gradient freezing. *Acs Sustain Chem Eng* 7:1381–1388. <https://doi.org/10.1021/acssuschemeng.8b05085>
4. Chen Y, Zhang L, Yang Y, Pang B et al (2021) Recent Progress on Nanocellulose Aerogels: Preparation, Modification, Composite Fabrication, Applications. *Adv Mater* 33:e2005569. <https://doi.org/10.1002/adma.202005569>
5. Cho SH, Jung S, Rinklebe J, Kwon EE (2021) CO₂-assisted catalytic pyrolysis of cellulose acetate using Ni-based catalysts. *Environmental pollution* (1987) 275:116667. <https://doi.org/10.1016/j.envpol.2021.116667>
6. Dai H, Huang H (2017) Enhanced Swelling and Responsive Properties of Pineapple Peel Carboxymethyl Cellulose-g-poly(acrylic acid-co-acrylamide) Superabsorbent Hydrogel by the Introduction of Carclazyte. *J Agr Food Chem* 65:565–574. <https://doi.org/10.1021/acs.jafc.6b04899>
7. Dai H, Ou S, Huang Y, Huang H (2018) Utilization of pineapple peel for production of nanocellulose and film application. *Cellulose (London)* 25:1743–1756. <https://doi.org/10.1007/s10570-018-1671-0>
8. Dai H, Huang Y, Zhang Y, Zhang H et al (2019) Green and facile fabrication of pineapple peel cellulose/magnetic diatomite hydrogels in ionic liquid for methylene blue adsorption. *Cellulose* 26:3825–3844. <https://doi.org/10.1007/s10570-019-02283-6>
9. Dai H, Zhang H, Ma L, Zhou H et al (2019) Green pH/magnetic sensitive hydrogels based on pineapple peel cellulose and polyvinyl alcohol: Synthesis, characterization and naringin prolonged release. *Carbohydr Polym* 209:51–61. <https://doi.org/10.1016/j.carbpol.2019.01.014>

10. Dai H, Huang Y, Zhang H, Ma L et al (2020) Direct fabrication of hierarchically processed pineapple peel hydrogels for efficient Congo red adsorption. *Carbohydr Polym* 230:115599. <https://doi.org/10.1016/j.carbpol.2019.115599>
11. Dai H, Wu J, Zhang H, Chen Y et al (2020) Recent advances on cellulose nanocrystals for Pickering emulsions: Development and challenge. *Trends Food Sci Tech* 102:16–29. <https://doi.org/10.1016/j.tifs.2020.05.016>
12. Dai H, Zhang H, Chen Y, Ma L et al (2021) Co-stabilization and properties regulation of Pickering emulsions by cellulose nanocrystals and nanofibrils from lemon seeds. *Food Hydrocolloid* 120:106884. <https://doi.org/10.1016/j.foodhyd.2021.106884>
13. Dai H, Chen Y, Zhang S, Feng X et al (2021) Enhanced interface properties and stability of lignocellulose nanocrystals stabilized pickering emulsions: The leading role of tannic acid. *J Agr Food Chem* 69:14650–14661. <https://doi.org/10.1021/acs.jafc.1c04930>
14. Dilamian M, Noroozi B (2021) Rice straw agri-waste for water pollutant adsorption: Relevant mesoporous super hydrophobic cellulose aerogel. *Carbohydr Polym* 251:117016. <https://doi.org/10.1016/j.carbpol.2020.117016>
15. Ding Q, Xu X, Yue Y, Mei C et al (2018) Nanocellulose-Mediated electroconductive Self-Healing hydrogels with high strength, plasticity, viscoelasticity, stretchability, and biocompatibility toward multifunctional applications. *Acs Appl Mater Inter* 10:27987–28002. <https://doi.org/10.1021/acsami.8b09656>
16. Fei Y, Liang M, Yan L, Chen Y et al (2020) Co/C@cellulose nanofiber aerogel derived from metal-organic frameworks for highly efficient electromagnetic interference shielding. *Chem Eng J* 392:124815. <https://doi.org/10.1016/j.cej.2020.124815>
17. Gómez FN, Combariza MY, Blanco-Tirado C (2016) Facile cellulose nanofibrils amidation using a 'one-pot' approach. *Cellulose* 24:717–730. <https://doi.org/10.1007/s10570-016-1174-9>
18. Gong C, Ni J, Tian C, Su Z (2021) Research in porous structure of cellulose aerogel made from cellulose nanofibrils. *Int J Biol Macromol* 172:573–579. <https://doi.org/10.1016/j.ijbiomac.2021.01.080>
19. Hassan SH, Velayutham TS, Chen YW, Lee HV (2021) TEMPO-oxidized nanocellulose films derived from coconut residues: Physicochemical, mechanical and electrical properties. *Int J Biol Macromol* 180:392–402. <https://doi.org/10.1016/j.ijbiomac.2021.03.066>
20. Huang C, Tu C, Lee R, Yang C et al (2019) Study of various diameter and functionality of TEMPO-oxidized cellulose nanofibers on paraquat adsorptions. *Polym Degrad Stabil* 161:206–212. <https://doi.org/10.1016/j.polymdegradstab.2019.01.023>
21. Huang P, Zhang P, Min L, Tang J et al (2020) Synthesis of cellulose carbon aerogel via combined technology of wet ball-milling and TEMPO-mediated oxidation and its supersorption performance to ionic dyes. *Bioresource Technol* 315:123815. <https://doi.org/10.1016/j.biortech.2020.123815>
22. Isogai A, Hänninen T, Fujisawa S, Saito T (2018) Review: Catalytic oxidation of cellulose with nitroxyl radicals under aqueous conditions. *Prog Polym Sci* 86:122–148.

<https://doi.org/10.1016/j.progpolymsci.2018.07.007>

23. Khan AS, Man Z, Bustam MA, Kait CF et al (2015) Impact of Ball-Milling pretreatment on pyrolysis behavior and kinetics of crystalline cellulose. *Waste Biomass Valori* 7:571–581.
<https://doi.org/10.1007/s12649-015-9460-6>
24. Kim H, Roy S, Rhim J (2021) Effects of various types of cellulose nanofibers on the physical properties of the CNF-based films. *J Environ Chem Eng* 9:106043.
<https://doi.org/10.1016/j.jece.2021.106043>
25. Lai C, Sheng L, Liao S, Xi T et al (2013) Surface characterization of TEMPO-oxidized bacterial cellulose: Modification of bacterial cellulose. *Surf Interface Anal* 45:1673–1679.
<https://doi.org/10.1002/sia.5306>
26. Lai C, Zhang S, Chen X, Sheng L (2014) Nanocomposite films based on TEMPO-mediated oxidized bacterial cellulose and chitosan. *Cellulose* 21:2757–2772. <https://doi.org/10.1007/s10570-014-0330-3>
27. Levanič J, Šenk VP, Nadrah P, Poljanšek I et al (2020) Analyzing TEMPO-Oxidized cellulose fiber morphology: New insights into optimization of the oxidation process and nanocellulose dispersion quality. *Acs Sustain Chem Eng* 8:17752–17762. <https://doi.org/10.1021/acssuschemeng.0c05989>
28. Li J, Bhattacharjee S, Ghoshal S (2015) The effects of viscosity of carboxymethyl cellulose on aggregation and transport of nanoscale zerovalent iron. *Colloids Surf A* 481:451–459.
<https://doi.org/10.1016/j.colsurfa.2015.05.023>
29. Li Z, Cheng X, He S, Shi X et al (2016) Aramid fibers reinforced silica aerogel composites with low thermal conductivity and improved mechanical performance. *Compos A Appl Sci Manuf* 84:316–325. <https://doi.org/10.1016/j.compositesa.2016.02.014>
30. Lin N, Bruzzese C, Dufresne A (2012) TEMPO-Oxidized nanocellulose participating as crosslinking aid for Alginate-Based sponges. *Acs Appl Mater Inter* 4:4948–4959.
<https://doi.org/10.1021/am301325r>
31. Liu H, Du H, Zheng T, Liu K et al (2021) Cellulose based composite foams and aerogels for advanced energy storage devices. *Chem Eng J* 426:130817. <https://doi.org/10.1016/j.cej.2021.130817>
32. Liu S, Liang H, Sun T, Yang D et al (2018) A recoverable dendritic polyamidoamine immobilized TEMPO for efficient catalytic oxidation of cellulose. *Carbohydr Polym* 202:563–570.
<https://doi.org/10.1016/j.carbpol.2018.09.016>
33. Lyu W, Li J, Zheng L, Liu H et al (2021) Fabrication of 3D compressible polyaniline/cellulose nanofiber aerogel for highly efficient removal of organic pollutants and its environmental-friendly regeneration by peroxydisulfate process. *Chem Eng journa* 414:128931.
<https://doi.org/10.1016/j.cej.2021.128931>
34. Malkin AY (2013) Non-Newtonian viscosity in steady-state shear flows. *J Non-Newton Fluid* 192:48–65. <https://doi.org/10.1016/j.jnnfm.2012.09.015>
35. Manzocco L, Plazzotta S, Powell J, de Vries A et al (2022) Structural characterisation and sorption capability of whey protein aerogels obtained by freeze-drying or supercritical drying. *Food*

- Hydrocolloid 122:107117. <https://doi.org/10.1016/j.foodhyd.2021.107117>
36. Masruchin N, Park B, Lee JM (2018) Surface modification of TEMPO-oxidized cellulose nanofibrils for composites to give color change in response to pH level. *Cellulose* 25:7079–7090. <https://doi.org/10.1007/s10570-018-2072-0>
 37. Mettu S, Hathi Z, Athukoralalage S, Priya A et al (2021) Perspective on constructing Cellulose-Hydrogel-Based Gut-Like bioreactors for growth and delivery of Multiple-Strain probiotic bacteria. *J Agr Food Chem* 69:4946–4959. <https://doi.org/10.1021/acs.jafc.1c00468>
 38. Mhd Haniffa MAC, Ching YC, Chuah CH, Yong Ching K et al (2017) Effect of TEMPO-oxidization and rapid cooling on thermo-structural properties of nanocellulose. *Carbohyd Polym* 173:91–99. <https://doi.org/10.1016/j.carbpol.2017.05.084>
 39. Miao X, Lin J, Tian F, Li X et al (2016) Cellulose nanofibrils extracted from the byproduct of cotton plant. *Carbohyd Polym* 136:841–850. <https://doi.org/10.1016/j.carbpol.2015.09.056>
 40. Mirtaghavi A, Baldwin A, Tanideh N, Zarei M et al (2020) Crosslinked porous three-dimensional cellulose nanofibers-gelatine biocomposite scaffolds for tissue regeneration. *Int J Biol Macromol* 164:1949–1959. <https://doi.org/10.1016/j.ijbiomac.2020.08.066>
 41. Payormhorm J, Idem R (2020) Synthesis of C-doped TiO₂ by sol-microwave method for photocatalytic conversion of glycerol to value-added chemicals under visible light. *Appl Catal Gen* 590:117362. <https://doi.org/10.1016/j.apcata.2019.117362>
 42. Perumal AB, Nambiar RB, Moses JA, Anandharamakrishnan C (2022) Nanocellulose: Recent trends and applications in the food industry. *Food Hydrocolloid* 127. <https://doi.org/10.1016/j.foodhyd.2022.107484>
 43. Perzon A, Jørgensen B, Ulvskov P (2020) Sustainable production of cellulose nanofiber gels and paper from sugar beet waste using enzymatic pre-treatment. *Carbohyd Polym* 230:115581. <https://doi.org/10.1016/j.carbpol.2019.115581>
 44. Poyraz B, Tozluoğlu A, Candan Z, Demir A et al (2018) TEMPO-treated CNF composites: Pulp and matrix effect. *Fiber Polym* 19:195–204. <https://doi.org/10.1007/s12221-018-7673-y>
 45. Qu R, Wang Y, Li D, Wang L (2021) The study of rheological properties and microstructure of carboxylated nanocellulose as influenced by level of carboxylation. *Food Hydrocolloid* 121:106985. <https://doi.org/10.1016/j.foodhyd.2021.106985>
 46. Qu R, Tang M, Wang Y, Li D et al (2021) TEMPO-oxidized cellulose fibers from wheat straw: Effect of ultrasonic pretreatment and concentration on structure and rheological properties of suspensions. *Carbohyd Polym* 255:117386. <https://doi.org/10.1016/j.carbpol.2020.117386>
 47. Segal L, Creely JJ, Martin AE, Conrad CM (1959) An empirical method for estimating the degree of crystallinity of native cellulose using the X-Ray diffractometer. *Text Res J* 29:786–794. <https://doi.org/10.1177/004051755902901003>
 48. Sehaqui H, Zhou Q, Berglund LA (2011) High-porosity aerogels of high specific surface area prepared from nanofibrillated cellulose (NFC). *Compos Sci Technol* 71:1593–1599. <https://doi.org/10.1016/j.compscitech.2011.07.003>

49. Shivamathi CS, Gunaseelan S, Soosai MR, Vignesh NS et al (2022) Process optimization and characterization of pectin derived from underexploited pineapple peel biowaste as a value-added product. *Food Hydrocolloid* 123:107141. <https://doi.org/10.1016/j.foodhyd.2021.107141>
50. Silva TCF, Habibi Y, Colodette JL, Elder T et al (2012) A fundamental investigation of the microarchitecture and mechanical properties of tempo-oxidized nanofibrillated cellulose (NFC)-based aerogels. *Cellulose* 19:1945–1956. <https://doi.org/10.1007/s10570-012-9761-x>
51. Sofla MRK, Brown RJ, Tsuzuki T, Rainey TJ (2016) A comparison of cellulose nanocrystals and cellulose nanofibres extracted from bagasse using acid and ball milling methods. *Adv Nat Sci NanoSci NanoTechnol* 7:35004. <https://doi.org/10.1088/2043-6262/7/3/035004>
52. Sun Y, Chu Y, Wu W, Xiao H (2021) Nanocellulose-based lightweight porous materials: A review. *Carbohyd Polym* 255:117489. <https://doi.org/10.1016/j.carbpol.2020.117489>
53. Tang Z, Li W, Lin X, Xiao H et al (2017) TEMPO-Oxidized cellulose with high degree of oxidation. *Polymers-Basel* 9:421. <https://doi.org/10.3390/polym9090421>
54. Van Hai L, Zhai L, Kim HC, Kim JW et al (2018) Cellulose nanofibers isolated by TEMPO-oxidation and aqueous counter collision methods. *Carbohyd Polym* 191:65–70. <https://doi.org/10.1016/j.carbpol.2018.03.008>
55. Wan C, Jiao Y, Wei S, Zhang L et al (2019) Functional nanocomposites from sustainable regenerated cellulose aerogels: A review. *Chem Eng J* 359:459–475. <https://doi.org/10.1016/j.cej.2018.11.115>
56. Wei B, Li H, Li Q, Wen Y et al (2017) Stabilization of foam lamella using novel Surface-Grafted Nanocellulose-Based nanofluids. *Langmuir* 33:5127–5139. <https://doi.org/10.1021/acs.langmuir.7b00387>
57. Yang G, Guangrui M, Ming H, Xinxiang J et al (2020) Application of cellulose nanofibril as a wet-end additive in papermaking: A brief review. *Paper and Biomaterials* 2:76–84
58. Yang W, Shang J, Sharma P, Li B et al (2019) Colloidal stability and aggregation kinetics of biochar colloids: Effects of pyrolysis temperature, cation type, and humic acid concentrations. *Sci Total Environ* 658:1306–1315. <https://doi.org/10.1016/j.scitotenv.2018.12.269>
59. Zhang F, Ren H, Tong G, Deng Y (2016) Ultra-lightweight poly (sodium acrylate) modified TEMPO-oxidized cellulose nanofibril aerogel spheres and their superabsorbent properties. *Cellulose* 23:3665–3676. <https://doi.org/10.1007/s10570-016-1041-8>
60. Zhao D, Yang F, Dai Y, Tao F et al (2017) Exploring crystalline structural variations of cellulose during pulp beating of tobacco stems. *Carbohyd Polym* 174:146–153. <https://doi.org/10.1016/j.carbpol.2017.06.060>

Figures

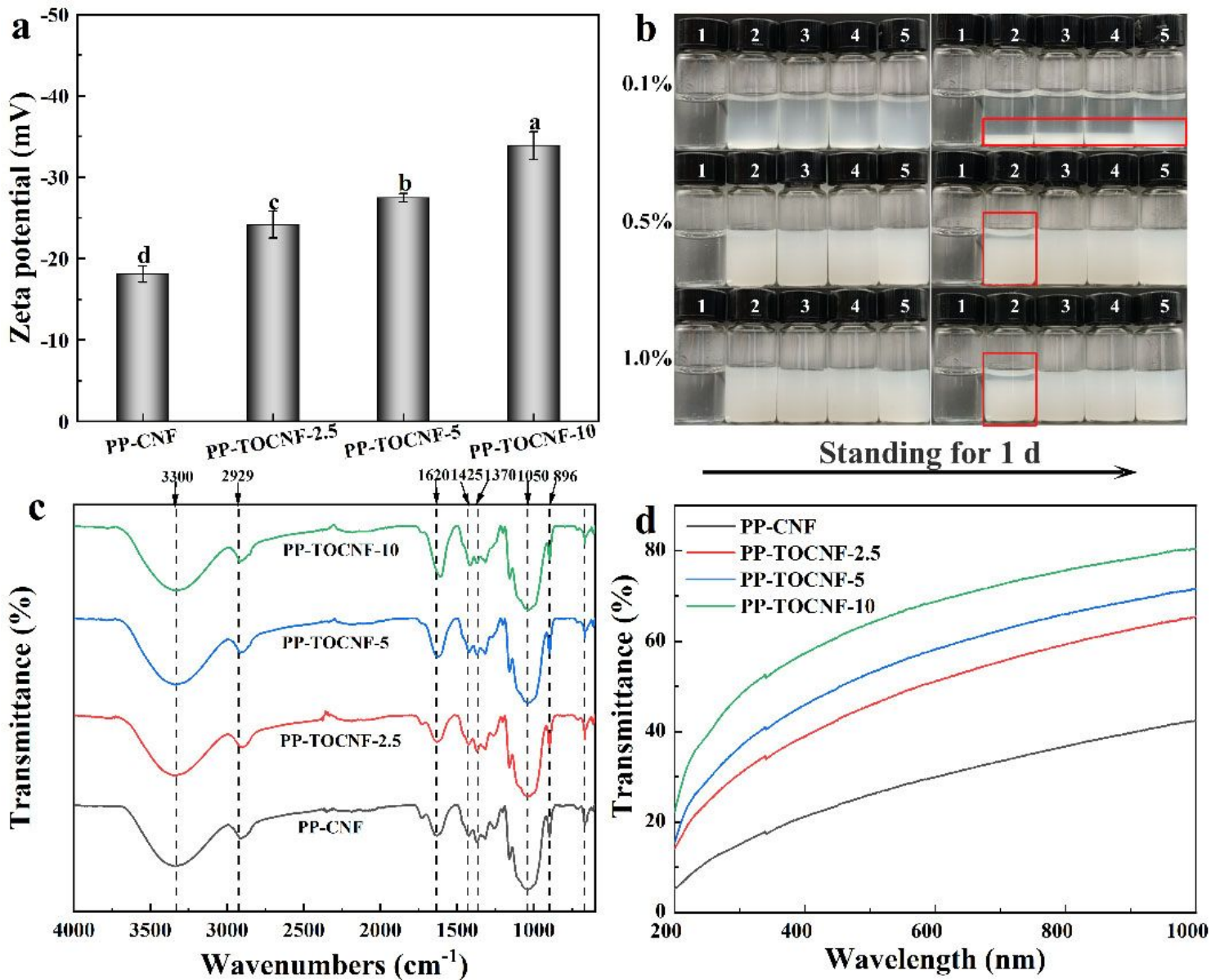


Figure 1

Zeta potential (a), appearance of sample suspensions before and after standing for 1 d (b); the number of 1-5 respectively represents the suspensions of H_2O (1), PP-CNF (2), PP-TOCNF-2.5 (3), PP-TOCNF-5 (4) and PP-TOCNF-10 (5); FTIR spectra (c); and UV-Vis light transmittance spectra of sample suspensions (d)

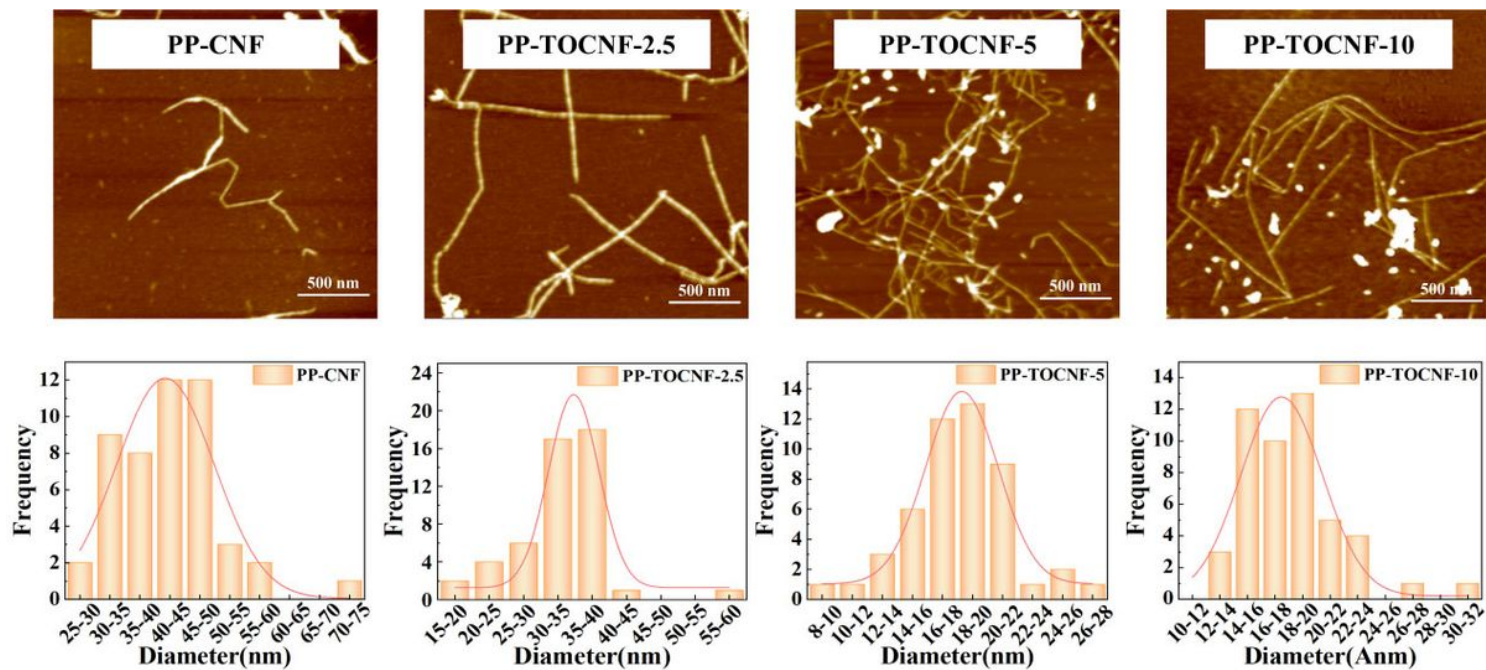


Figure 2

AFM images and diameter distributions of PP-CNF, PP-TOCNF-2.5, PP-TOCNF-5 and PP-TOCNF-10

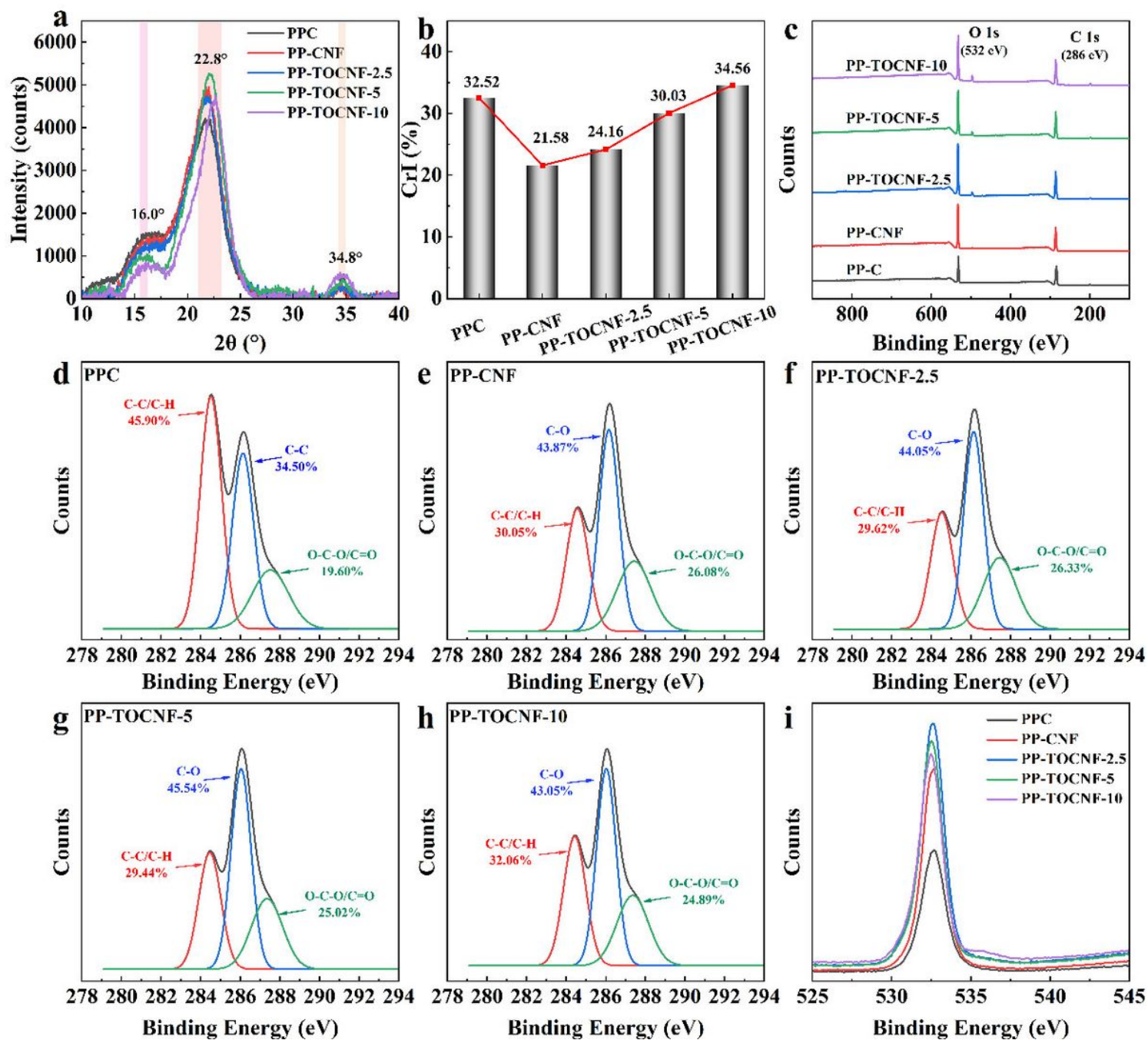


Figure 3

XRD patterns (a), the CrI (b); the XPS (c), the peak-fitted high-resolution C 1s (d-h) and overlaid high-res envelope regions of O 1s (i) for PPC, PP-CNF, PP-TOCNF-2.5, PP-TOCNF-5 and PP-TOCNF-10

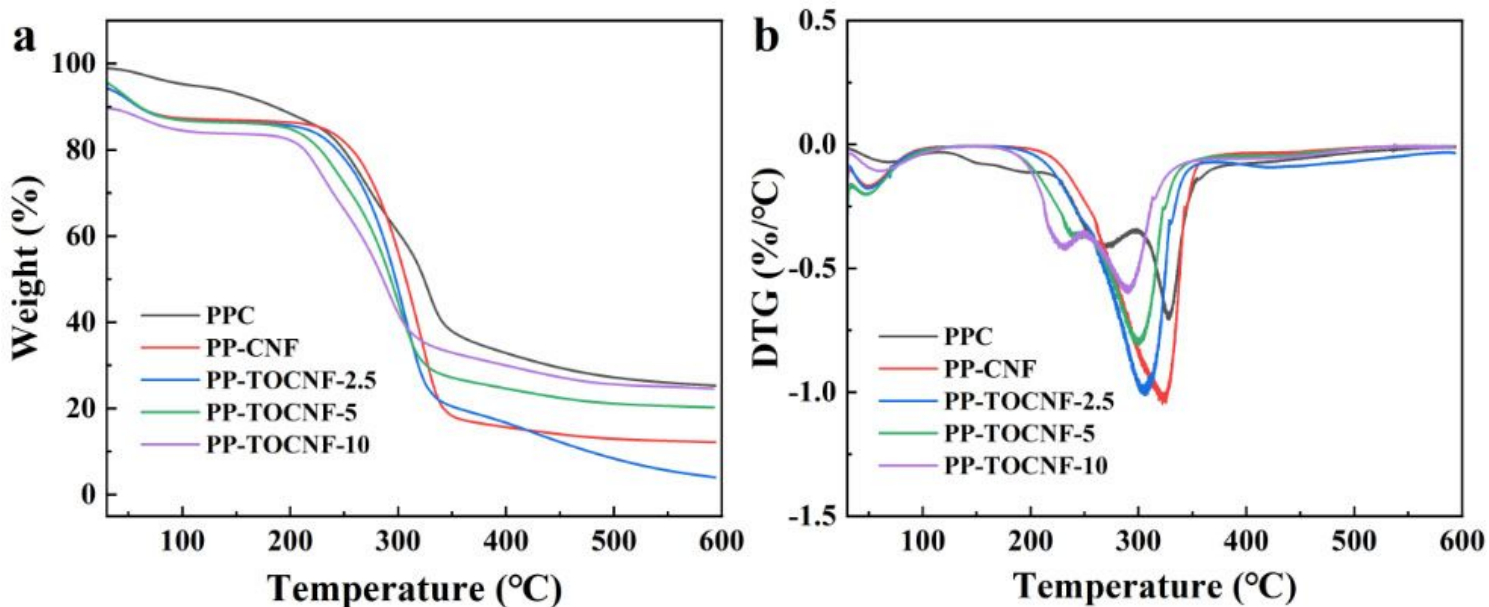


Figure 4

Thermogravimetric analysis (TGA) (a) and derivative thermogravimetric analysis (DTG) (b) curves of PPC, PP-CNF, PP-TOCNF-2.5, PP-TOCNF-5 and PP-TOCNF-10

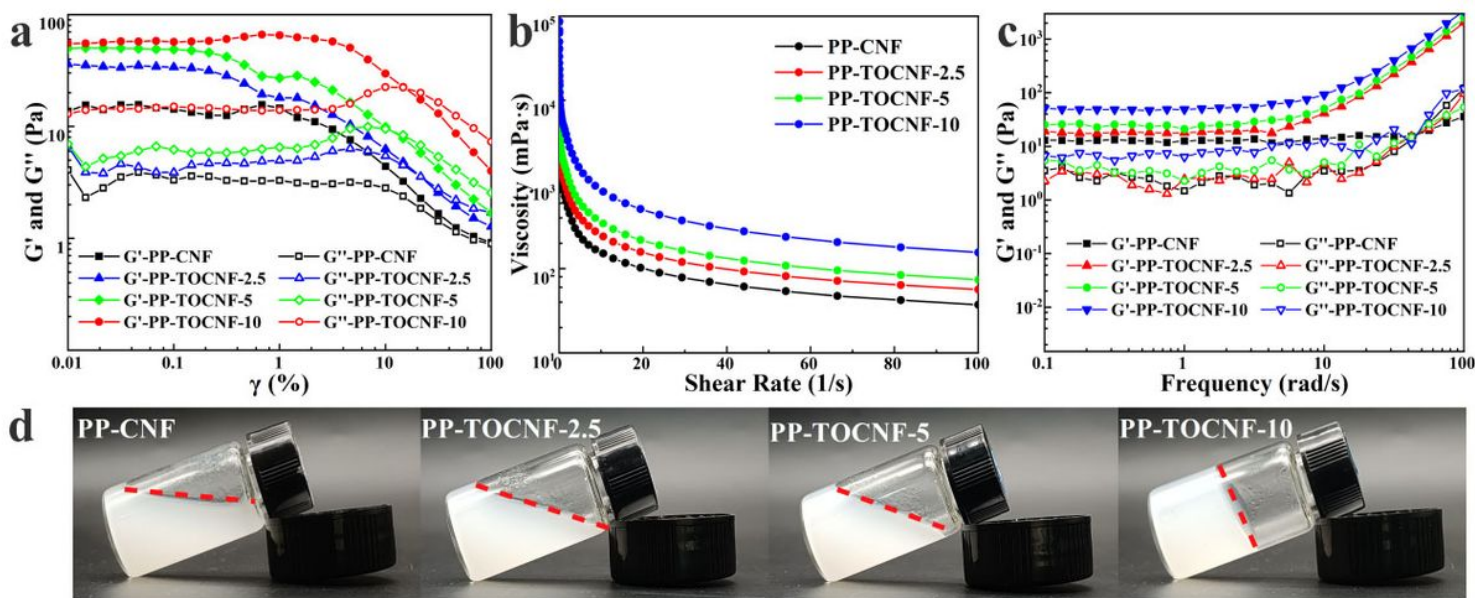


Figure 5

Rheological properties (a-c) and digital images of PP-CNF, PP-TOCNF-2.5, PP-TOCNF-5 and PP-TOCNF-10 suspensions (1.0 wt%)

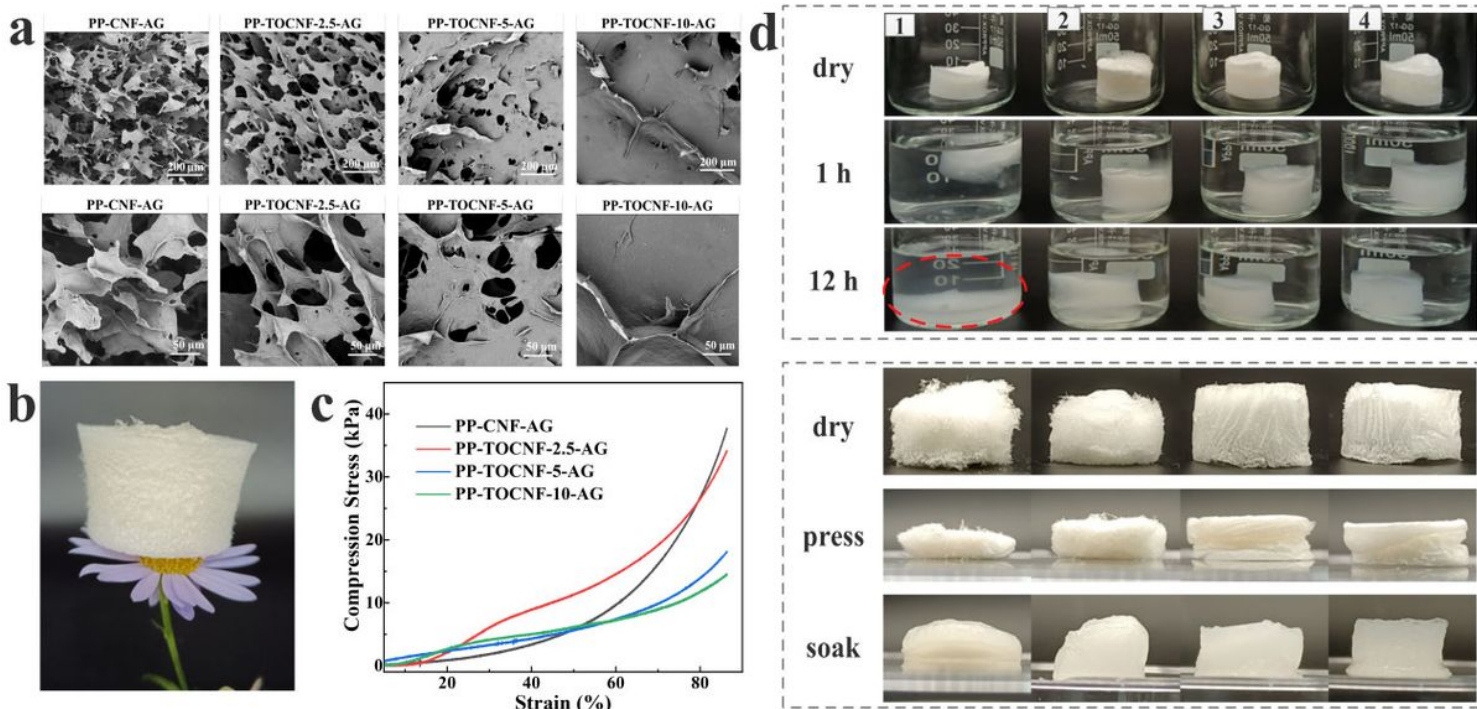


Figure 6

SEM images (a) (300× and 1000×), the digital images (b) and stress-strain curves (c) of obtained aerogels (PP-CNF-AG, PP-TOCNF-2.5-AG, PP-TOCNF-5-AG and PP-TOCNF-10-AG); Digital images (d) of water solubility and compressed rehydration of aerogel

Supplementary Files

This is a list of supplementary files associated with this preprint. Click to download.

- [GA.jpg](#)
- [Vedio.mp4](#)